18F-FDOPA PET for the Noninvasive Prediction of Glioma Molecular Parameters: A Radiomics Study

Timothée Zaragori[1,2], Julien Oster[2], Véronique Roch[1], Gabriela Hossu[2,3], Mohammad B. Chawki[1], Rachel Grignon[1], Celso Pouget[4,5], Guillaume Gauchotte[4,5], Fabien Rech[6,7], Marie Blonski[7,8], Luc Taillandier[7,8], Laëtitia Imbert[1,2], and Antoine Verger[1,2]

[1]Department of Nuclear Medicine and Nancyclotep Imaging Platform, CHRU-Nancy, Université de Lorraine, Nancy, France; [2]IADI UMR 1254, INSERM, Université de Lorraine, Nancy, France; [3]CIC 1433 Innovation Technologique, INSERM, CHRU-Nancy, Université de Lorraine, Nancy, France; [4]Department of Pathology, CHRU-Nancy, Université de Lorraine, Nancy, France; [5]INSERM U1256, Université de Lorraine, Nancy, France; [6]Department of Neurosurgery, CHRU-Nancy, Université de Lorraine, Nancy, France; [7]Centre de Recherche en Automatique de Nancy CRAN UMR 7039, CNRS, Université de Lorraine, Nancy, France; and [8]Department of Neuro-Oncology, CHRU-Nancy, Université de Lorraine, Nancy, France

The assessment of gliomas by 18F-FDOPA PET imaging as an adjunct to MRI showed high performance by combining static and dynamic features to noninvasively predict the isocitrate dehydrogenase (IDH) mutations and the 1p/19q codeletion, which the World Health Organization classified as significant parameters in 2016. The current study evaluated whether other 18F-FDOPA PET radiomics features further improve performance and the contributions of each of these features to performance. **Methods:** Our study included 72 retrospectively selected, newly diagnosed glioma patients with 18F-FDOPA PET dynamic acquisitions. A set of 114 features, including conventional static features and dynamic features, as well as other radiomics features, were extracted and machine-learning models trained to predict IDH mutations and the 1p/19q codeletion. Models were based on a machine-learning algorithm built from stable, relevant, and uncorrelated features selected by hierarchic clustering followed by a bootstrapped feature selection process. Models were assessed by comparing area under the curve using a nested cross-validation approach. Feature importance was assessed using Shapley additive explanations values. **Results:** The best models were able to predict IDH mutations (logistic regression with L2 regularization) and the 1p/19q codeletion (support vector machine with radial basis function kernel) with an area under the curve of 0.831 (95% CI, 0.790–0.873) and 0.724 (95% CI, 0.669–0.782), respectively. For the prediction of IDH mutations, dynamic features were the most important features in the model (time to peak, 35.5%). In contrast, other radiomics features were the most useful for predicting the 1p/19q codeletion (up to 14.5% of importance for the small-zone low-gray-level emphasis). **Conclusion:** 18F-FDOPA PET is an effective tool for the noninvasive prediction of glioma molecular parameters using a full set of amino-acid PET radiomics features. The contribution of each feature set shows the importance of systematically integrating dynamic acquisition for prediction of the IDH mutations as well as developing the use of radiomics features in routine practice for prediction of the 1p/19q codeletion.

Key Words: 18F-FDOPA PET; radiomics; glioma; machine learning; WHO 2016 classification

The World Health Organization (WHO) 2016 classification of gliomas shifted from a purely histology-based approach (*1*) to the integration of molecular parameters (*2*). These parameters notably include isocitrate dehydrogenase (IDH) mutations and the 1p/19q codeletion, which are determinant in the patient's prognosis (*3*).

PET imaging using radiolabeled amino acids is currently recommended as an adjunct to MRI by the Response Assessment in Neuro-Oncology group (*4*), with the ability to noninvasively predict molecular parameters using, among others, 6-18F-fluoro-L-DOPA (18F-FDOPA) (*5*). One advantage of such an image-derived noninvasive prediction is the ability to study the metabolism of the whole tumor area, whereas histopathologic analyses consider only part of the tumor. In a recent series of 58 newly diagnosed gliomas, 18F-FDOPA PET imaging was found to predict IDH mutational status with an accuracy of 74% thanks to the integration of dynamic features (*5*).

The non-invasive predictive capability of dynamic amino-acid PET correlated with the emergence of the radiomics field, which extracts numerous quantitative features from images on the basis of classic static and dynamic features (*5*) but also others, such as morphologic and textural features (*6*). These radiomics studies helped to noninvasively predict specific tumor phenotypes by using machine learning algorithms to identify advanced imaging biomarkers representative of the intratumoral heterogeneity (*7*).

Radiomics is increasingly being used in the PET characterization of gliomas at the initial diagnosis (*8*), even though only a minority of studies to date has been performed with the amino-acid tracers recommended for glioma assessment (*9–11*). It has therefore become paramount to understand the potential significance of particular imaging features—that is, static, dynamic, and other radiomics features—to predict IDH mutations and the 1p/19q codeletion. To the best of our knowledge, in the age of radiomics no study has yet assessed the potential benefits of amino-acid PET imaging to characterize the molecular parameters of gliomas according to the WHO 2016 classification by exploiting amino-acid PET acquisition as a whole.

The current study therefore aimed to determine to what extent the high-throughput extraction of advanced imaging biomarkers can predict these molecular parameters and the contributions of each of these ^{18}F-FDOPA PET features to performance.

MATERIALS AND METHODS

Patients

We retrospectively selected newly diagnosed glioma patients who were investigated by ^{18}F-FDOPA PET for suspected glioma components in the Department of Nuclear Medicine at the CHRU of Nancy, between November 2012 and November 2019. Only included patients satisfying the following selection criteria were included: patients with a neuropathologic diagnosis of grade II, III, or IV glioma according to the WHO 2016 classification (2) with a maximum delay from the time of the ^{18}F-FDOPA PET of 150 d for diffuse grade II or III glioma and 60 d for glioblastoma, in line with previously published time ranges (5,12,13); patients with a dynamic analysis and available raw data; and patients with visually abnormal ^{18}F-FDOPA uptake, that is, by excluding isometabolic and photopenic gliomas (14,15). A flowchart of patient selection is shown in Figure 1. The institutional ethics committee (Comité d'Ethique du CHRU de Nancy) approved the evaluation of retrospective patient data on August 26, 2020. The trial was registered at ClinicalTrials.gov (NCT04469244). This research complied with the principles of the Declaration of Helsinki. Informed consent was obtained from all individuals included in the study.

^{18}F-FDOPA PET Acquisition and Image Reconstruction

Patients were instructed to fast for at least 4 h before the examination, and some patients were administered carbidopa 1 h before the examination to increase uptake of the tracer in the brain (16). Patients were scanned on a conventional PET/CT camera (Biograph 6 True Point; Siemens Healthineers) and on a digital PET/CT camera (Vereos; Philips). A CT scan was first recorded for each patient, immediately followed by a 30-min 3-dimensional list-mode PET recording initiated during the bolus injection of 3 MBq (conventional) or 2 MBq (digital) of ^{18}F-FDOPA per kilogram of body weight. Dynamic PET images consisted of 30 frames of 1 min each, whereas static PET images were reconstructed from the list-mode data acquired 10–30 min after injection (Fig. 2) (10,17).

The conventional PET/CT static and dynamic images were reconstructed using the ordered-subsets expectation maximization 2-dimensional algorithm (2 iterations, 21 subsets, 4-mm gaussian postreconstruction filter) without time-of-flight information and 256 × 256 × 148 voxels of 2.7 × 2.7 × 3 mm with a slice spacing of 1.5 mm for the static and dynamic images. The digital static images were reconstructed using the time-of-flight information and a high-resolution protocol with the ordered-subsets expectation maximization 3-dimensional algorithm (2 iterations, 10 subsets, a deconvolution of the point-spread function) and 256 × 256 × 164 voxels of 1 × 1 × 1 mm, whereas a protocol with a lower spatial resolution was used for the dynamic images in order to limit the level of noise—that is, 3 iterations, 15 subsets, without point-spread function, and 128 × 128 × 82 voxels of 2 × 2 × 2 mm (18).

All images were corrected for attenuation using CT, dead time, random coincidences, and scattered coincidences during the reconstruction process.

Segmentation

Volumes of interest (VOIs) for tumor, contralateral healthy brain, and striatum were defined on the static image using LifeX software (lifexsoft.org) (19).

This healthy brain uptake was measured in a crescent-shaped VOI manually positioned on the unaffected hemisphere so as to comprise both white and gray matter, as recommended (10).

Tumor VOI was segmented semiautomatically using a threshold of 1.6 for healthy brain SUV_{mean} (10). The striatum was delineated semiautomatically using a threshold of 70% of the SUV_{max} ^{18}F-FDOPA uptake and corrected manually when required.

When a VOI comprised multiple components, the one with the largest volume was retained in the analysis. All final VOIs were visually inspected by an experienced physician to ensure the quality of the methods applied. Examples of representative VOIs are provided in Figure 2.

Image Preprocessing and Extraction of Features

Figure 2 illustrates the workflow of image preprocessing and the extraction of features.

Static Features. Mean, maximum, and peak tumor–to–normal-brain ratios and tumor-to-striatum ratios were computed as, respectively, SUV_{mean}, SUV_{max}, and SUV_{peak} in the tumor VOI divided by the SUV_{mean} in the brain and the striatum VOI. The metabolic tumor volume was defined as the volume of the tumor VOI.

Dynamic Features. Each dynamic frame was first registered to the associated CT image, in order to correct for any potential patient movement during the acquisition (20). The brain and tumor time–activity curves were extracted by retrieving the SUV_{mean} for each frame, respectively, in the brain VOI and in the volume corresponding to the SUV_{peak} of the tumor VOI on the static image, to represent the most aggressive part of the tumor (21). To overcome noise effects, a nonlinear fit was applied to each time–activity curve (5,22), with a function dedicated to tumoral vascularization (patent WO/2008/053268, entitled "Method and System for Quantification of Tumoral Vascularization") and a nonlinear least optimization using the trust-region–reflective algorithm. Given that tumor–to–normal-brain values are less likely to be influenced by carbidopa premedication than is SUV, the time–activity curve ratio, representing the evolution of the ratio between the tumor- and brain-fitted time–activity curves, was calculated (5). Time to peak was computed as the delay between the beginning of the dynamic acquisition and the time of the maximum uptake value, and the slope of the linear regression of the data between the 10th and 30th minutes was then determined (5).

Other Radiomics Features. For patients whose acquisition was performed on the conventional PET camera, isotropic voxel resampling was performed using the SimpleITK Python package following Image Biomarker Standardization Initiative recommendations to reach a voxel size of 2.7 × 2.7 × 2.7 mm with tricubic spline interpolation. Each static image was normalized by the SUV_{mean} in the brain VOI to compensate for differences in carbidopa premedication in our population—differences that are known to impact SUV measurements (23). A fixed bin size of 0.1 was used for absolute image discretization in all patients. One hundred five features were extracted from the tumor VOI, including morphologic, local intensity, intensity-based statistical, intensity histogram, and textural features. A 3-dimensional merging strategy was used for textural matrices (24). Extraction of the features was based on the guidelines and benchmark values of the Image Biomarker Standardization Initiative (24) using pyradiomics (https://github.com/Radiomics/pyradiomics) or an in-house software for local intensity features that were not available in pyradiomics. The full list of extracted features is given in Supplemental Table 1, and extraction parameters are given in Supplemental Table 2 (supplemental materials are available at http://jnm.snmjournals.org).

These 114 features were used for the following classification tasks: IDH mutant (IDH-positive) versus IDH wild-type (IDH-negative)
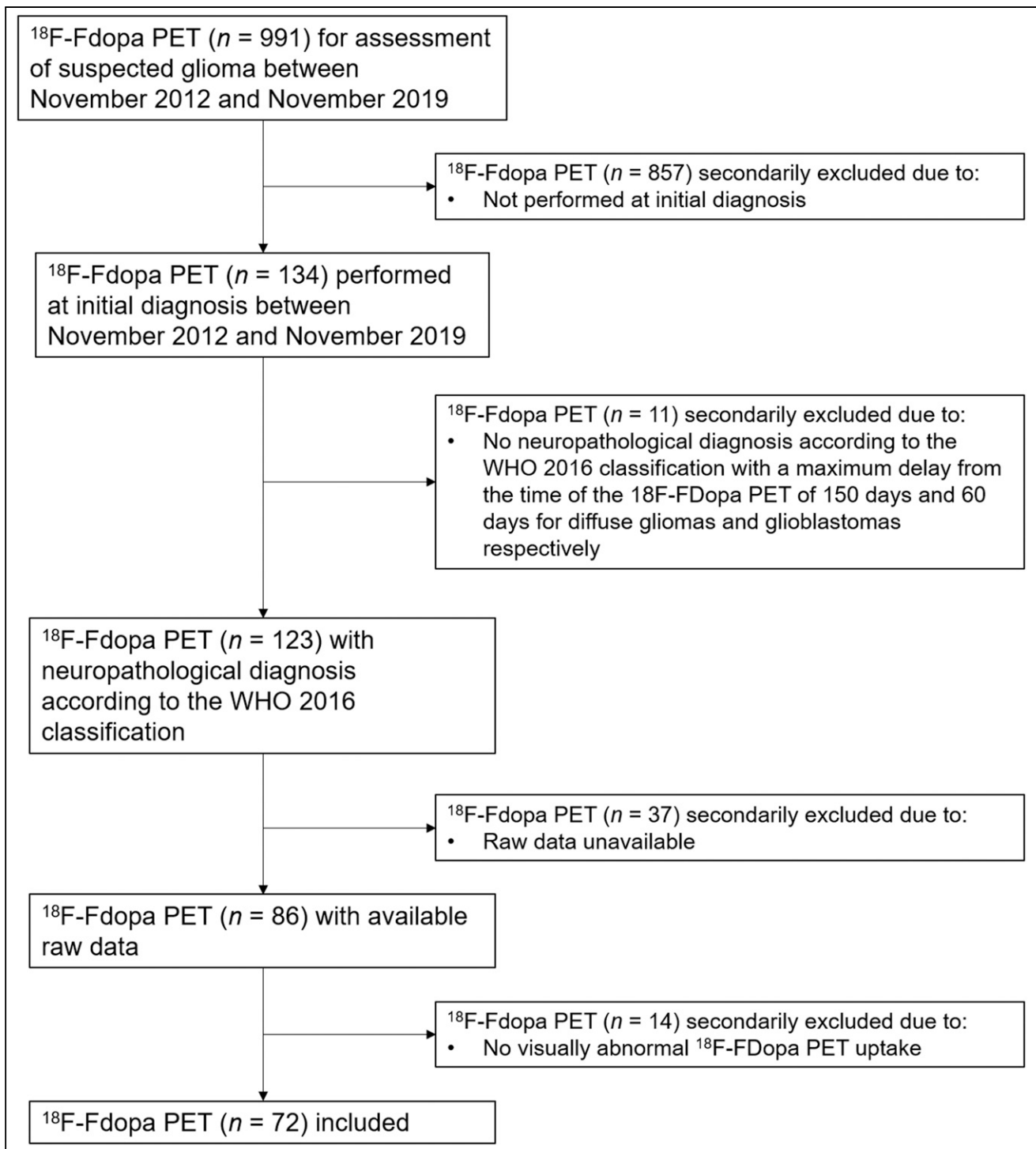
FIGURE 1. Flowchart of retrospective selection of study patients.

gliomas, and gliomas with and without 1p/19q codeletion (1p19q-positive vs. 1p19q-negative).

Data Harmonization

All extracted features other than dynamic features were harmonized with the modified ComBat method (http://github.com/SteinCK/M-ComBat) (*25*) using the digital PET device as a reference. This harmonization proved to be efficient for removing the device effect without altering the biologic variation

(*26*). Dynamic features were not harmonized since they represent semiquantitative kinetic features and are not much affected by the PET device (*9*).

Model Building

For a given training and validation set, all transformations and the algorithm were fitted using the training set only. In the validation set, all transformations computed on the training set were applied and the fitted algorithm was used to predict the output.
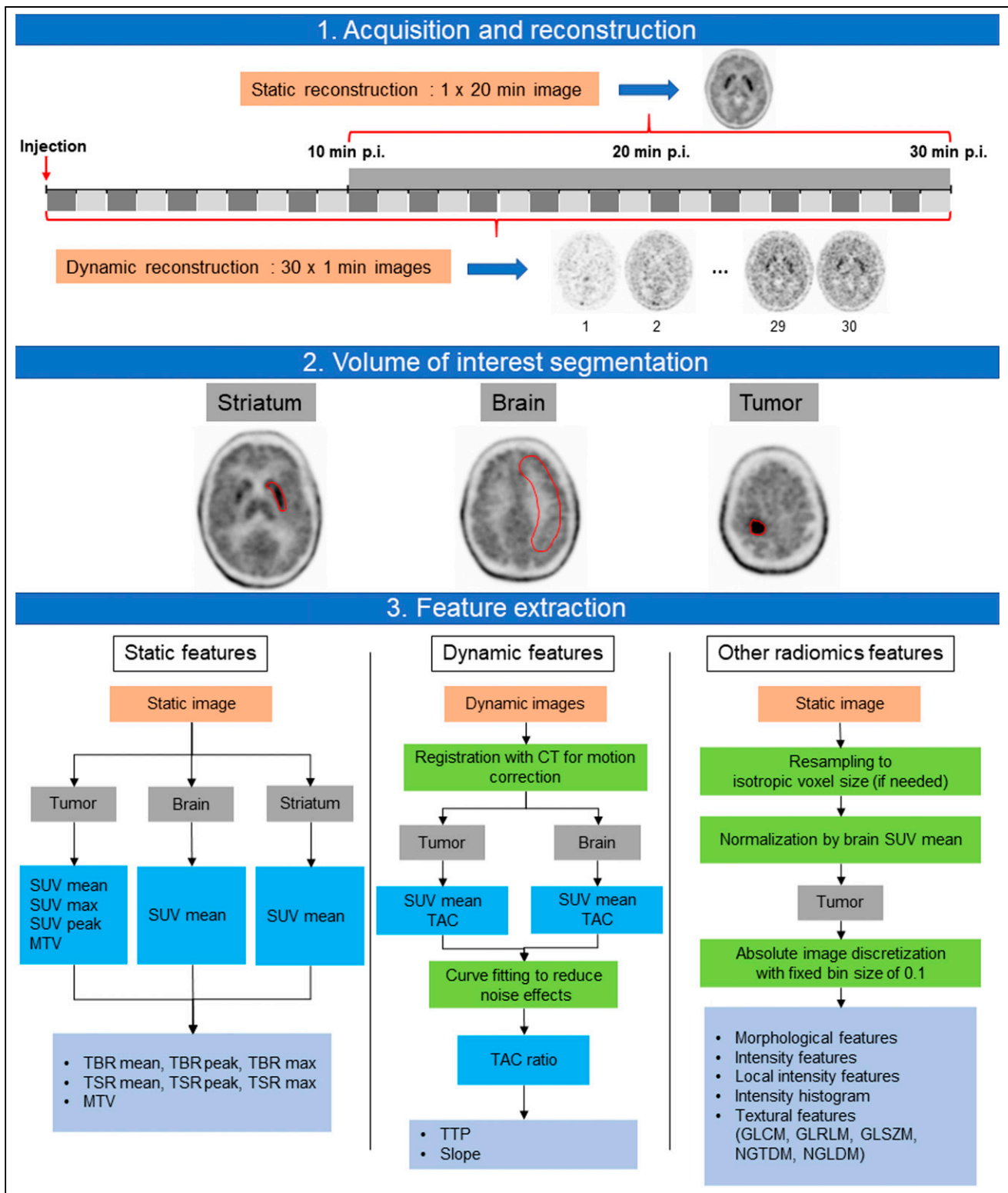
FIGURE 2. Detailed workflow of image acquisition and reconstruction, VOI segmentation (shown in red contours), and features extracted, where images and VOIs are listed in orange and gray rectangles, respectively, processing steps in green rectangles, intermediate results in dark blue rectangles, and final features in light blue rectangles. GLCM = gray level co-occurrence matrix; GLRLM = gray level run length matrix; GLSZM = gray level size zone matrix; MTV = metabolic tumor volume; NGTDM = neighborhood gray tone difference matrix; NGLDM = neighboring gray level dependence; p.i. = after injection; TBR = tumor–to–normal-brain ratio; TSR = tumor-to-striatum ratio; TAC = time–activity curve; TTP = time to peak.

All static, dynamic, and other features were first normalized with a z score normalization. Then, dimensionality was reduced by hierarchic clustering (27), where highly correlated features (absolute Spearman correlation coefficient $\geq$ 0.9) are clustered together. For each cluster, the feature selected was the medoid of the cluster, that is, the feature that minimizes the dissimilarity from all other features in the cluster. The most relevant and stable uncorrelated features were selected on the basis of 100 bootstrap samples in which the features were ranked using the Wilcoxon score (28), with a global rank computed with the previously published importance score (27). A range of 5–15 selected features was tested, in increments of 5.

Finally, selected features were given as an input to a machine learning classification algorithm. Class imbalance for each classification task was addressed by assigning weights inversely related to the class's prevalence in the training data during machine-learning algorithm training. In the case of severely imbalanced groups in a given classification task (classification of 1p/19q codeletion), the Synthetic Minority Oversampling Technique algorithm (29) was used for oversampling the minority class. The performance of 5 classifiers implemented were compared: logistic regression with L2 regularization, neural networks, random forest, support vector machine with radial basis function kernel, and support vector machine with linear kernel.

Model Performance

Nested cross-validation was used to get an unbiased estimate of the model's performance (30), with repeated stratified cross-validations as inner and outer loops to reduce the influence of the variance on the results (31). Hyperparameters were tuned through an inner loop with a 3-fold stratified cross-validation repeated 50 times by optimizing the mean area under the curve (AUC) overall inner folds and using 100 iterations of a random search over the set of hyperparameters described in Supplemental Table 3. The model assessment was performed through the outer loop with a 10-fold stratified cross-validation repeated 5 times by calculating the mean AUC overall outer folds. For this purpose, software was developed in-house and is freely available online (https://github.com/TimZaragori/Sklearn_NestedCV/tree/master/Radiomics_gliomas_article). The whole modeling pipeline is shown in Figure 3. For each classification task, the final model selected was the one with the highest performance.

Statistical Analysis

Categoric variables are expressed as percentages, and continuous variables as medians (first to third quartiles), because variables did not follow a normal distribution. Groups were compared with the χ^2 test for categoric variables and the Mann–Whitney test for continuous variables. For each outer fold receiver-operating-characteristic curve, the optimal threshold was computed on the training set by selecting the point on the curve closest to (0,1) and applying it on the validation set to get the predictions. Diagnostic performance (accuracy, sensitivity, specificity, positive predictive value, and negative predictive value) was computed from outer model predictions. P values lower than 0.05 were considered significant. One thousand bootstrap iterations of outer results were used to determine the 95% CIs of each dataset performance. Analyses were performed with R software, version 3.6.2 (R Foundation for Statistical Computing). For each classification, the model introspection was performed using Shapley additive explanation (SHAP) values (32), which provide information on the importance of each feature by taking into account the whole modeling pipeline. SHAP values were computed on each outer model and concatenated to obtain a global and reliable importance score for each feature.

RESULTS

Patients

We retrospectively selected 72 patients (median 51.0 [interquartile range (IQR), 34.8-62.4 y]; 29 women), who underwent ^{18}F-FDOPA PET for a newly diagnosed glioma, with a histopathologic diagnosis determined either from tissue obtained during surgery ($n = 33$) or from biopsies ($n = 39$): 43 IDH-positive gliomas from which 18 1p/19q codeleted. The time window between PET imaging and neuropathologic confirmation was 35 d (IQR, 11.5–84 d) for diffuse grade II or III gliomas and 3 d (IQR, 1–24 d) for glioblastomas. Data for 44 of the patients (61%) were acquired by conventional PET/CT, and data for 28 (39%) were acquired by digital PET/CT. Forty-two (58%) patients were premedicated with carbidopa. The patients who underwent the conventional PET/CT were already analyzed previously (5). Further details of the patient characteristics are provided in Table 1. The validations of the harmonization and normalization processes are shown in, respectively, Supplemental Tables 4 and 5.

Predicting IDH Mutations

The combination of logistic regression with L2 regularization and 5 selected features was the best-performing model for predicting IDH mutations and yielded an AUC of 0.831 (95% CI, 0.790–0.873) (details of the predictive performance of this model and the performance of all models for predicting IDH mutations are presented in Table 2 and Supplemental Fig. 1, respectively). The time to peak was found to be the feature with the highest importance, reaching a 35.5% contribution to the overall model's performance (Fig. 4). The other dynamic parameter, slope, was also among the 5 most contributive features, even though with a lower importance (4.3%).

Predicting the 1p/19q Codeletion

The 1p/19q codeletion was best predicted by a model that combined a support vector machine with a radial basis function kernel and 15 features selected (AUC, 0.724 [95% CI, 0.669–0.782]) (Supplemental Fig. 2 shows the results of all models for 1p/19q codeletion, and Table 2 shows the complete predictive performance of this model). In contrast to the prediction of the IDH mutations, the other radiomics features were the most contributive, with the small-zone low-gray-level emphasis from gray level size zone matrix being the most important feature (14.5%) (Fig. 4).

An overview of the impact on the model of each feature according to its values for the interpretation of the radiomics signatures is shown in Figure 5. Representative examples of patients for both classifications, with their local interpretation using SHAP values, are provided in Figure 6.

DISCUSSION

The current study shows that ^{18}F-FDOPA PET imaging is an efficient tool for the noninvasive prediction of two of the most important molecular parameters of newly diagnosed gliomas according to the WHO 2016 classification, the IDH mutations using dynamic features and the 1p/19q codeletion using other radiomics features. Using a set of 114 radiomics features, a good performance for predicting these 2 parameters was achieved, with AUCs of 0.831 and 0.724, respectively. Interestingly, the greatest contribution to the predictive performance for IDH mutations was provided by dynamic features, whereas the contribution of the set of other radiomics
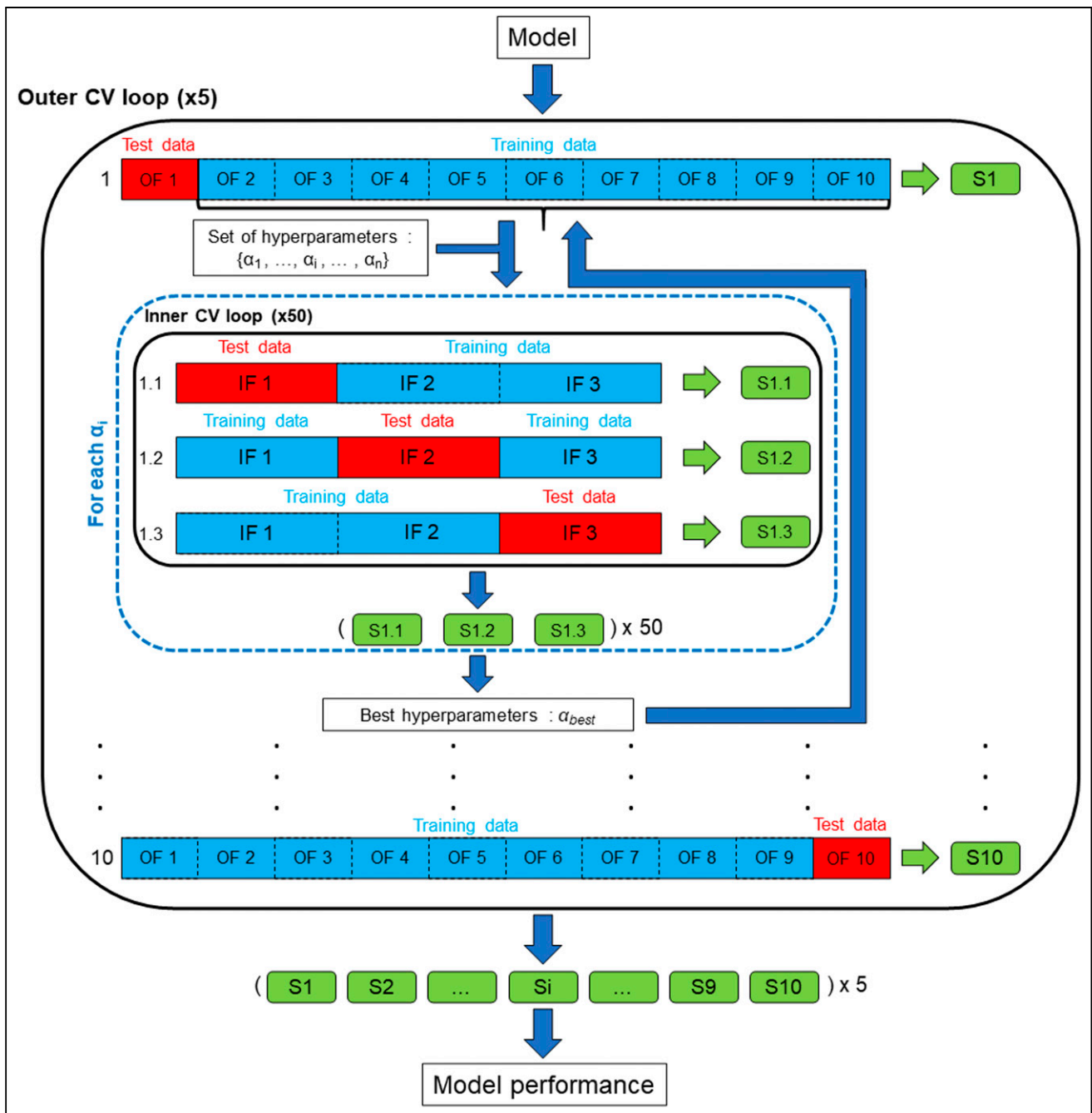
FIGURE 3. Modeling pipeline using nested cross-validation to obtain unbiased estimate of model performance. Fifty repeats of 3-fold cross-validation were used as inner loop and 5 repeats of 10-fold cross-validation as outer loop. For each fold of outer cross-validation, hyperparameters of model were tuned in inner cross-validation using only outer training data. Best hyperparameters chosen were then used to fit model to outer training data, and model performance was evaluated on outer test data. Blue and red rectangles, respectively, denote training and test data for each cross-validation. Green arrows represent predictions made by fitted model on test data, and green boxes represent score calculated from these predictions. CV = cross-validation; OF = outer fold; IF = inner fold; Si = score on test data of outer fold i; Si.j = score on test data of inner fold j from outer fold i.

features was the most useful for predicting the 1p/19q codeletion (Table 2; Figs. 4 and 5).

Since the emergence of the radiomics field, only a few amino-acid PET studies have been devoted to the characterization of molecular parameters in newly diagnosed gliomas (8). Among these, only two were performed for the 2 molecular parameters that are key features of the WHO 2016 classification. Lohmann et al. (9) focused their analysis

exclusively on predicting IDH genotype, whereas Haubold et al. extended their analysis to various other molecular parameters using MR fingerprints and ^{18}F-FET but did not include the information provided by the dynamic PET acquisitions (11). The objective of our study was to predict the classification of newly diagnosed gliomas according to both IDH mutations and the 1p/19q codeletion by considering amino-acid PET data as a whole—that is, by extracting a full set of radiomics

TABLE 1
Patient Characteristics (*n* = 75)

Characteristic	Conventional (*n* = 44)	Digital (*n* = 28)	All (*n* = 72)	*P*
Age (y)				0.020*
Median	42.4	57.2	51.0	
Range	19.8–73.7	20.3–78.6	19.8–78.6	
Female sex	15 (34)	14 (50)	29 (40)	0.273
Primary histopathologic type				0.305
Astrocytoma, IDH-mutant	10 (23)	7 (25)	17 (24)	
Anaplastic astrocytoma, IDH-mutant	5 (11)	1 (4)	6 (8)	
Astrocytoma, IDH-wild-type	2 (5)	3 (11)	5 (7)	
Anaplastic astrocytoma, IDH-wild-type	2 (5)	3 (11)	5 (7)	
Oligodendroglioma, IDH-mutant and 1p/19q codeleted	7 (16)	4 (14)	11 (15)	
Anaplastic oligodendroglioma, IDH-mutant and 1p/19q codeleted	7 (16)	0 (0)	7 (10)	
Glioblastoma, IDH-wild-type	10 (23)	9 (32)	19 (26)	
Glioblastoma, IDH-mutant	1 (2)	1 (4)	2 (3)	
Carbidopa premedication	14 (32)	28 (100)	42 (58)	<0.001*
Contrast enhancement on MRI	18 (41)	11 (39)	29 (40)	1

*$P < 0.05$ for comparison between conventional PET and digital PET patients.
Data are number followed by percentage in parentheses, except for age.

TABLE 2
Model Performances for Each Classification

Classification	AUC	Sensitivity (%)	Specificity (%)	Accuracy (%)	PPV (%)	NPV (%)
IDH-positive vs. IDH-negative (LR_L2 and 5 features selected)	0.831 (0.790–0.873)	77.0 (72.5–81.4)	70.7 (63.0–78.3)	74.7 (71.4–78.4)	82.5 (78.5–86.7)	70.9 (64.9–76.6)
1p19q-positive vs. 1p19q-negative (SVM_RBF and 15 features selected)	0.724 (0.669–0.782)	55.0 (43.0–66.0)	72.3 (66.7–78.5)	67.0 (62.5–71.2)	39.6 (30.4–48.3)	84.2 (80.5–88.2)

PPV = positive predictive value; NPV = negative predictive value; IDH-positive = IDH mutant gliomas; IDH-negative = IDH wild-type gliomas; LR_L2 = logistic regression with L2 regularization algorithm; 1p19q-positive = 1p/19q codeleted gliomas; 1p19q-negative = gliomas not 1p/19q codeleted; SVM_RBF = support vector machine with radial basis function kernel algorithm.
Data are mean followed by 95% CI in parentheses.

features, including dynamic ones, to better characterize the contribution of each group of features (static, dynamic, and other radiomics features) in the prediction of molecular parameters.

For the prediction of IDH mutations, our results are consistent with those of Lohmann et al. using dynamic ^{18}F-FET, who reported accuracies of greater than 70% (*9*) (vs. 74.7% in the present study). Conversely, Haubold et al. reported lower predictive performances for IDH mutations (AUC of 0.639, vs. 0.831 in the present study) but without including any dynamic information

in their analyses (*11*). This latter point underlines the fact that dynamic information is crucial for the prediction of IDH mutations, consistent with our previous results, in which dynamic features led to accuracies of up to 74% in predicting IDH mutations (*5*). For the prediction of the 1p/19q codeletion, the set of other radiomics features provided the most important contribution (Figs. 4 and 5). These statements are supported by the findings of Haubold et al., who reported a much higher prediction of the textural features for the classification of the 1p/19q
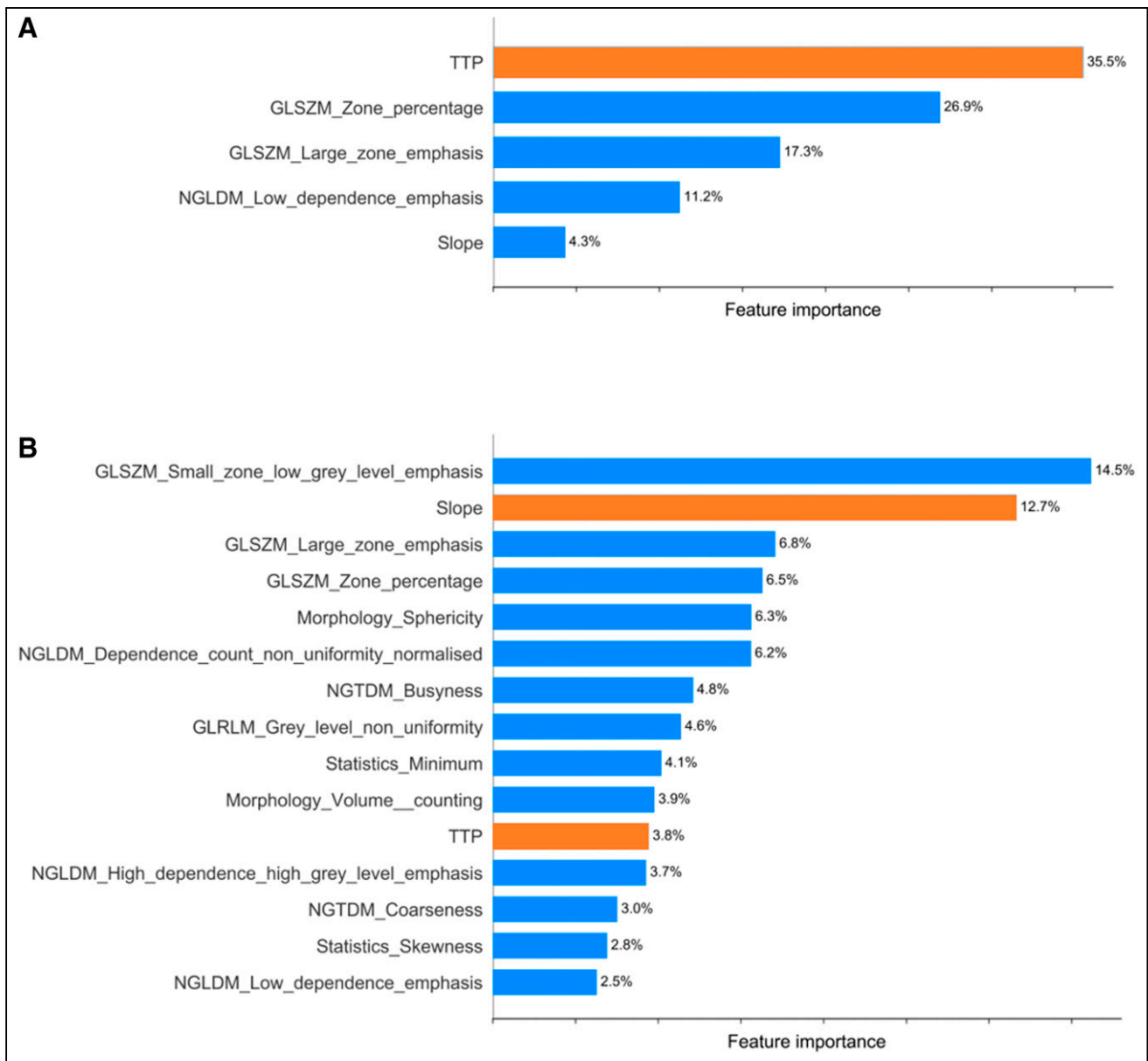
FIGURE 4. Feature importance derived from outer models for most contributive features to prediction of IDH mutations using logistic regression with L2 regularization and 5 features selected (A) and 1p/19q codeletion using support vector machine with radial basis function kernel and 15 features selected (B). Individual importance of each feature was normalized to sum of 1.0. Other radiomic features are in blue, and dynamic features are in orange.

codeletion (AUC of 0.858) than IDH mutations (AUC of 0.639). The highly predictive value of dynamic parameters for IDH mutations and other radiomics features for 1p/19q codeletion is further supported by additional results obtained when comparing the performances of the 114-feature dataset with the datasets having only static features, static and other radiomics features, and static and dynamic features (Supplemental Fig. 3).

It is crucial to try and explain glioma signatures in terms of the significance of the selected features (Figs. 4 and 5). In the signature of the IDH mutations, IDH wild-type gliomas are characterized by low time-to-peak values. This is consistent with results from our previous study (5), in which IDH wild-type gliomas, reputed as more aggressive tumors, were associated with a breakdown of the blood–brain barrier but also a higher microvessel density and LAT1

expression. All these considerations are consistent with intense wash-in and washout phenomena, leading to short times to peak.

The signature interpretation for the 1p/19q codeletion classification is more complex and can be considered in 2 parts. The first is by focusing on features that have highly negative SHAP values and that help the classifier exclude a potential 1p19q-positive glioma. This is the case for high values of minimum intensity statistics, given that 1p19q-positive gliomas exhibit high amino-acid PET uptake (33), as well as low values of small-zone low-gray-level emphasis from gray level size zone matrix and high values of busyness from neighborhood gray tone difference matrix, since 1p19q-positive gliomas are homogeneous tumors. Second, and in contrast to the first interpretation of the signature, features exhibiting positive SHAP values allow the
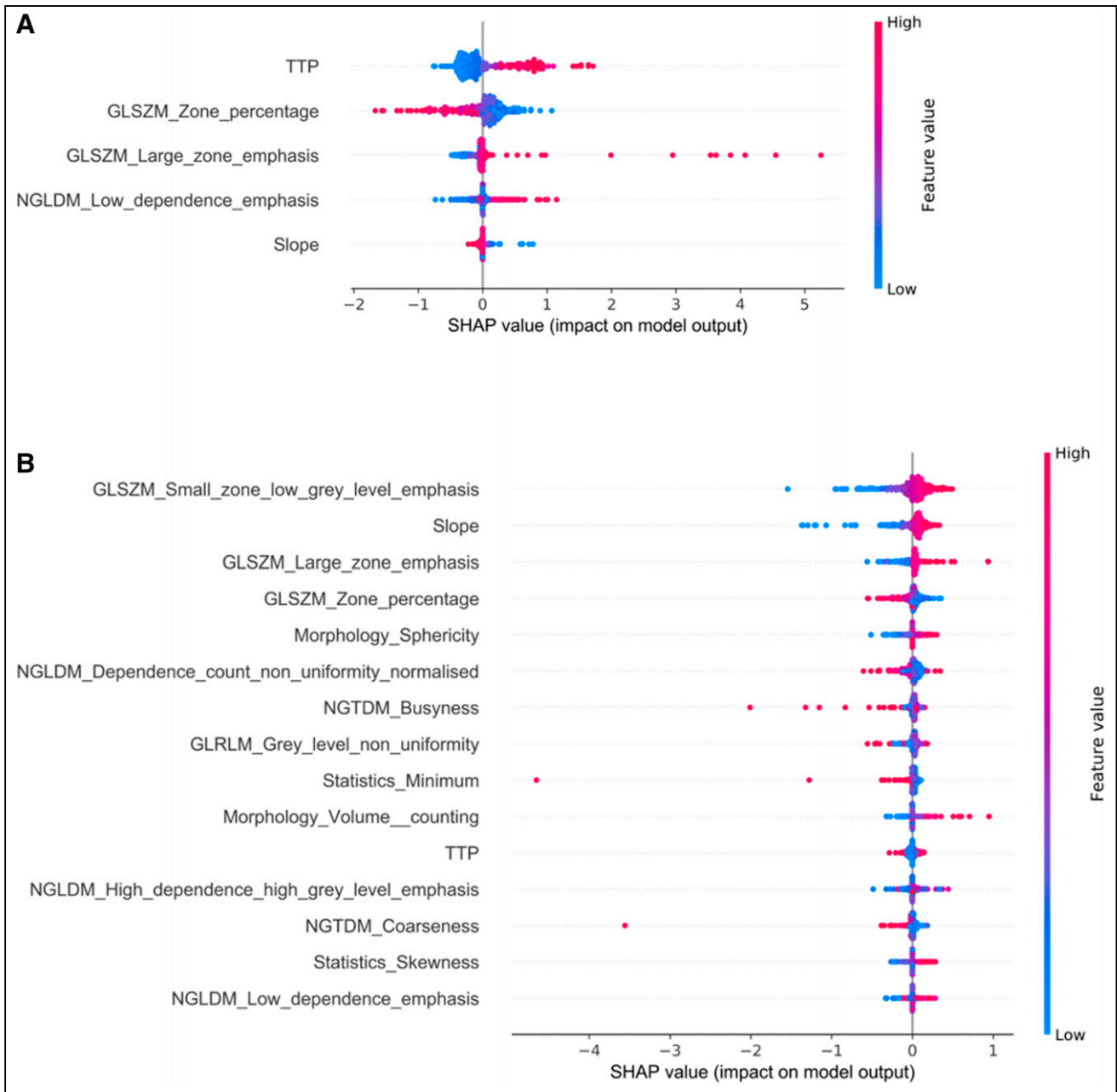
FIGURE 5. Overview of impact on model of each feature according to its values (for prediction of IDH mutations [A] and for prediction of 1p/19q codeletion [B]). Impact on model output is shown with SHAP values on x-axis, and feature value is displayed in colors (blue and red for, respectively, low and high values). For instance, in A, for classification of IDH mutations, high values of time to peak (in red) are showing positive SHAP values and thus are associated with prediction of positive class (IDH-positive gliomas) as opposed to low values of time to peak (in blue), which exhibit negative SHAP values, meaning that they are associated with prediction of negative class (IDH-negative gliomas).

classifier to confirm a potential 1p19q-positive glioma. This is the case for features associated with a nonaggressive behavior such as high values of sphericity morphologic feature, characterizing spheric tumors or other features from the gray level size zone matrix representative of a homogeneous tumor (high values of large-zone emphasis and low values of zone percentage).

As a limitation, the number of patients was relatively low, particularly the number of glioma patients with 1p/19 codeletions, even though the number was comparable to and even larger than that of other radiomics studies performed on this relatively rare

entity (*9,11*). Our methodology for radiomics modeling (feature selection, nested cross-validation, and adapted corrections for imbalanced datasets) was nevertheless adapted to the number of patients to avoid the risk of overfitting. However, validation on an external dataset of the suggested models is still required before transfer to the clinical setting. Another limitation is the use of 2 different PET cameras for acquisitions—a factor that we handled by harmonizing the features of each device using the modified ComBat method (Supplemental Table 4). In contrast to the ComBat method, the modified method has the advantage of aligning data in the space
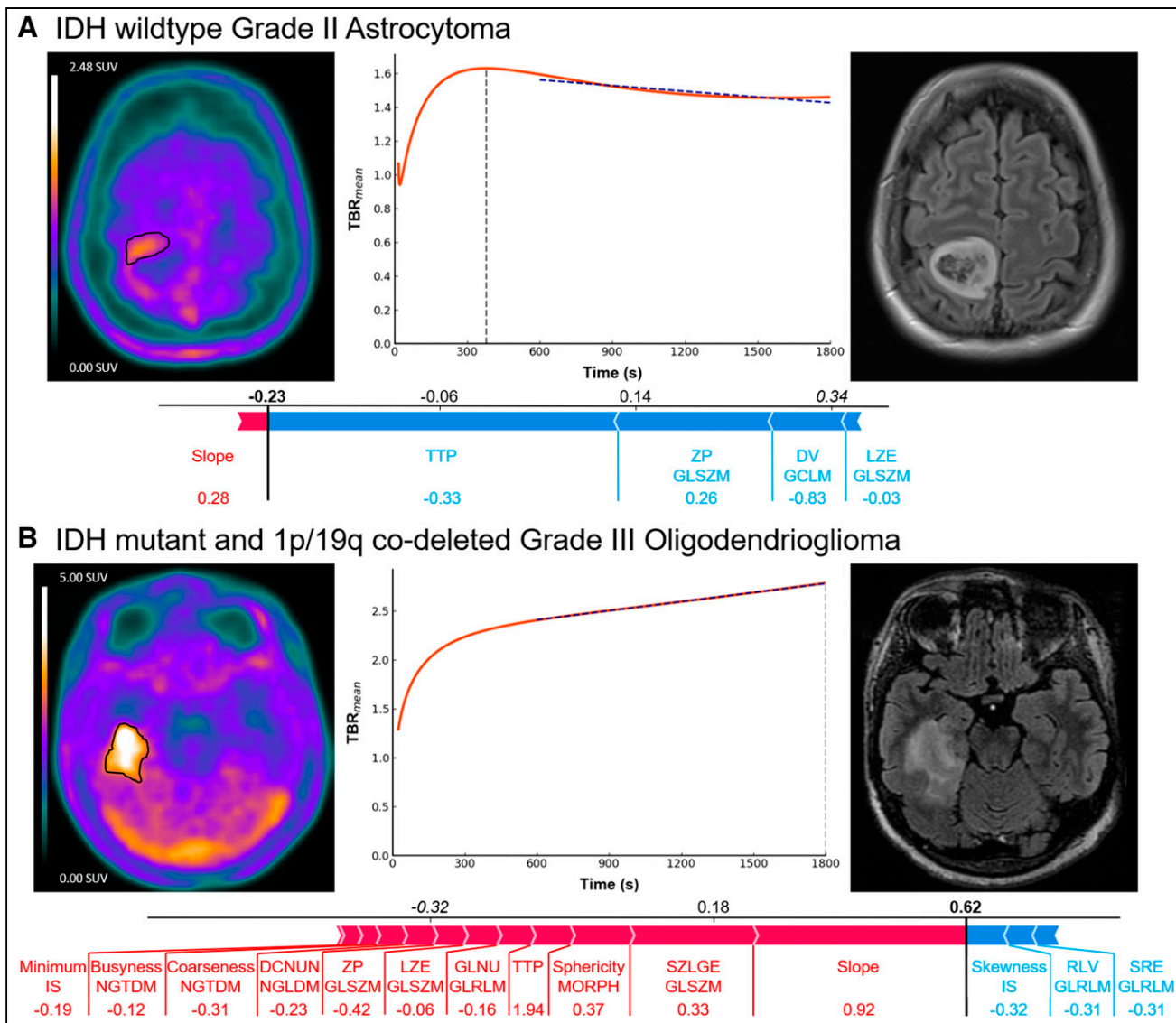
FIGURE 6. Representative examples of patients with IDH wild-type glioma (A) and 1p/19q codeleted glioma (B). Shown for each patient are axial slice of ^{18}F-FDOPA PET (left), dynamic mean tumor–to–normal-brain ratio curve (middle; time to peak, light gray dotted line; slope, dark blue dotted line), and same slice on FLAIR MRI (right), above graphic representing contribution of features involved in model prediction (IDH mutations classification [A]; 1p/19q codeletion classification [B]). Red features push prediction toward positive class, whereas blue features push toward negative class; longer arrow indicates more impact on model. Base model values (value of featureless model) and final decision values are displayed, respectively, in italics and boldface. For interpretation purposes, feature names along with their value (expressed in z score) are displayed under each arrow. TTP = time to peak; ZP = zone percentage; DV = difference variance; LZE = large-zone emphasis; SZLGE = small-zone low-gray-level emphasis; GLNU = gray-level nonuniformity; DCNUN = dependence count nonuniformity normalized. IS = intensity statistics; GLCM = gray level co-occurrence matrix; GLRLM = gray level run length matrix; GLSZM = gray level size zone matrix; MORPH = morphologic; NGTDM = neighborhood gray tone difference matrix; NGLDM = neighboring gray level dependence matrix.

of a specific device so that results can be used in routine clinical practice.

CONCLUSION

To the best of our knowledge, our current study was the first to focus on predicting the presence of major molecular parameters that are of prognostic interest, based on the WHO 2016 glioma classification, by using a full set of amino-acid PET static, dynamic, and radiomics features. Interestingly, most of the salient information for the prediction of IDH mutations is provided by the dynamic analysis, which highlights the necessity of systematically including dynamic acquisition as part of routine amino-acid PET imaging. However, for the classification of the 1p/19q codeletion, the predominant contribution of textural features shows the need to develop the routine extraction of such features through machine learning models as complementary tools for clinical interpretation.

DISCLOSURE

No potential conflict of interest relevant to this article was reported.

KEY POINTS

QUESTION: To what extent can the high-throughput extraction of advanced imaging biomarkers predict molecular parameters in gliomas, and what is the contribution of each ^{18}F-FDOPA PET feature to the performance?

PERTINENT FINDINGS: ^{18}F-FDOPA PET is an effective tool for the noninvasive prediction of glioma molecular parameters using a full set of amino-acid PET radiomics features, with respective AUCs of 0.831 (95% CI, 0.790–0.873) and 0.724 (95% CI, 0.669–0.782) for IDH mutations (dynamic features) and the 1p/19q codeletion (radiomics features).

IMPLICATIONS FOR PATIENT CARE: The contribution of each feature set shows the importance of systematically integrating the dynamic acquisition and of developing the use of radiomics features in clinical ^{18}F-FDOPA PET imaging.

REFERENCES

1. Louis DN, Ohgaki H, Wiestler OD, et al. The 2007 WHO classification of tumours of the central nervous system. *Acta Neuropathol (Berl).* 2007;114:97–109.
2. Louis DN, Perry A, Reifenberger G, et al. The 2016 World Health Organization classification of tumors of the central nervous system: a summary. *Acta Neuropathol (Berl).* 2016;131:803–820.
3. Eckel-Passow JE, Lachance DH, Molinaro AM, et al. Glioma groups based on 1p/19q, IDH, and TERT promoter mutations in tumors. *N Engl J Med.* 2015;372:2499–2508.
4. Albert NL, Weller M, Suchorska B, et al. Response Assessment in Neuro-Oncology working group and European Association for Neuro-Oncology recommendations for the clinical use of PET imaging in gliomas. *Neuro Oncol.* 2016;18:1199–1208.
5. Ginet M, Zaragori T, Marie P-Y, et al. Integration of dynamic parameters in the analysis of ^{18}F-FDopa PET imaging improves the prediction of molecular features of gliomas. *Eur J Nucl Med Mol Imaging.* 2020;47:1381–1390.
6. Visvikis D, Cheze Le Rest C, Jaouen V, Hatt M. Artificial intelligence, machine (deep) learning and radio(geno)mics: definitions and nuclear medicine imaging applications. *Eur J Nucl Med Mol Imaging.* 2019;46:2630–2637.
7. Aerts HJWL, Velazquez ER, Leijenaar RTH, et al. Decoding tumour phenotype by noninvasive imaging using a quantitative radiomics approach. *Nat Commun.* 2014;5:4006.
8. Lohmann P, Galldiks N, Kocher M, et al. Radiomics in neuro-oncology: basics, workflow, and applications. *Methods.* 2021;188:112–121.
9. Lohmann P, Lerche C, Bauer EK, et al. Predicting IDH genotype in gliomas using FET PET radiomics. *Sci Rep.* 2018;8:13328.
10. Law I, Albert NL, Arbizu J, et al. Joint EANM/EANO/RANO practice guidelines/SNMMI procedure standards for imaging of gliomas using PET with radiolabelled amino acids and [^{18}F]FDG: version 1.0. *Eur J Nucl Med Mol Imaging.* 2019;46:540–557.
11. Haubold J, Demircioglu A, Gratz M, et al. Non-invasive tumor decoding and phenotyping of cerebral gliomas utilizing multiparametric ^{18}F-FET PET-MRI and MR fingerprinting. *Eur J Nucl Med Mol Imaging.* 2020;47:1435–1445.
12. Verger A, Stoffels G, Bauer EK, et al. Static and dynamic ^{18}F–FET PET for the characterization of gliomas defined by IDH and 1p/19q status. *Eur J Nucl Med Mol Imaging.* 2018;45:443–451.
13. Fueger BJ, Czernin J, Cloughesy T, et al. Correlation of 6-^{18}F-fluoro-L-dopa PET uptake with proliferation and tumor grade in newly diagnosed and recurrent gliomas. *J Nucl Med.* 2010;51:1532–1538.
14. Galldiks N, Unterrainer M, Judov N, et al. Photopenic defects on O-(2-[^{18}F]-fluoroethyl)-L-tyrosine PET: clinical relevance in glioma patients. *Neuro Oncol.* 2019;21:1331–1338.
15. Zaragori T, Castello A, Guedj E, et al. Photopenic defects in gliomas with amino-acid PET and relative prognostic value: a multicentric ^{11}C-methionine and ^{18}F-FDOPA PET experience. *Clin Nucl Med.* 2021;46:e36–e37.
16. Schiepers C, Chen W, Cloughesy T, Dahlbom M, Huang S-C. ^{18}F-FDOPA kinetics in brain tumors. *J Nucl Med.* 2007;48:1651–1661.
17. Janvier L, Olivier P, Blonski M, et al. Correlation of SUV-derived indices with tumoral aggressiveness of gliomas in static ^{18}F-FDOPA PET: use in clinical practice. *Clin Nucl Med.* 2015;40:e429–e435.
18. Salvadori J, Imbert L, Perrin M, et al. Head-to-head comparison of image quality between brain ^{18}F-FDG images recorded with a fully digital versus a last-generation analog PET camera. *EJNMMI Res.* 2019;9:61.
19. Nioche C, Orlhac F, Boughdad S, et al. LIFEx: a freeware for radiomic feature calculation in multimodality imaging to accelerate advances in the characterization of tumor heterogeneity. *Cancer Res.* 2018;78:4786–4789.
20. Ye H, Wong K-P, Wardak M, et al. Automated movement correction for dynamic PET/CT Images: evaluation with phantom and patient data. *PLoS One.* 2014;9:e103745.
21. Pafundi DH, Laack NN, Youland RS, et al. Biopsy validation of ^{18}F-DOPA PET and biodistribution in gliomas for neurosurgical planning and radiotherapy target delineation: results of a prospective pilot study. *Neuro Oncol.* 2013;15:1058–1067.
22. Zaragori T, Ginet M, Marie P-Y, et al. Use of static and dynamic [^{18}F]-F-DOPA PET parameters for detecting patients with glioma recurrence or progression. *EJNMMI Res.* 2020;10:56.
23. Hoffman JM, Melega WP, Hawk TC, et al. The effects of carbidopa administration on 6-[^{18}F]fluoro-L-dopa kinetics in positron emission tomography. *J Nucl Med.* 1992;33:1472–1477.
24. Zwanenburg A, Vallières M, Abdalah MA, et al. The Image Biomarker Standardization Initiative: standardized quantitative radiomics for high-throughput image-based phenotyping. *Radiology.* 2020;295:328–338.
25. Stein CK, Qu P, Epstein J, et al. Removing batch effects from purified plasma cell gene expression microarrays with modified ComBat. *BMC Bioinformatics.* 2015;16:63.
26. Orlhac F, Boughdad S, Philippe C, et al. A postreconstruction harmonization method for multicenter radiomic studies in PET. *J Nucl Med.* 2018;59:1321–1328.
27. Leger S, Zwanenburg A, Pilz K, et al. A comparative study of machine learning methods for time-to-event survival data for radiomics risk modelling. *Sci Rep.* 2017;7:13206.
28. Parmar C, Grossmann P, Bussink J, Lambin P, Aerts HJWL. Machine learning methods for quantitative radiomic biomarkers. *Sci Rep.* 2015;5:13087.
29. Chawla NV, Bowyer KW, Hall LO, Kegelmeyer WP. SMOTE: Synthetic Minority Over-sampling Technique. *J Artif Intell Res.* 2002;16:321–357.
30. Cawley GC, Talbot NLC. On over-fitting in model selection and subsequent selection bias in performance evaluation. *J Mach Learn Res.* 2010;11:2079–2107.
31. Krstajic D, Buturovic LJ, Leahy DE, Thomas S. Cross-validation pitfalls when selecting and assessing regression and classification models. *J Cheminform.* 2014;6:10.
32. Lundberg SM, Lee S-I. A unified approach to interpreting model predictions. *Adv Neural Inf Process Syst.* 2017;30:4765–4774.
33. Jansen NL, Schwartz C, Graute V, et al. Prediction of oligodendroglial histology and LOH 1p/19q using dynamic [^{18}F]FET-PET imaging in intracranial WHO grade II and III gliomas. *Neuro Oncol.* 2012;14:1473–1480.